



HAL
open science

Determination of calibration parameters of cantilevers of arbitrary shape by finite element analysis

Jorge Rodriguez-Ramos, Felix Rico

► **To cite this version:**

Jorge Rodriguez-Ramos, Felix Rico. Determination of calibration parameters of cantilevers of arbitrary shape by finite element analysis. *Review of Scientific Instruments*, 2021, 92 (4), pp.045001. 10.1063/5.0036263 . hal-03207488

HAL Id: hal-03207488

<https://amu.hal.science/hal-03207488>

Submitted on 25 Apr 2021

HAL is a multi-disciplinary open access archive for the deposit and dissemination of scientific research documents, whether they are published or not. The documents may come from teaching and research institutions in France or abroad, or from public or private research centers.

L'archive ouverte pluridisciplinaire **HAL**, est destinée au dépôt et à la diffusion de documents scientifiques de niveau recherche, publiés ou non, émanant des établissements d'enseignement et de recherche français ou étrangers, des laboratoires publics ou privés.

1 **Determination of Calibration Parameters of Cantilevers of Arbitrary Shape** 2 **by Finite Elements Analysis**

3 Jorge Rodriguez-Ramos* and Felix Rico

4 *Aix-Marseille University, INSERM, CNRS, LAI,*

5 *13009 Marseille, France*

6 **Abstract**

7 The use of atomic force microscopy on nanomechanical measurements requires accurate calibration of
8 the cantilever's spring constant (k_c) and the optical lever sensitivity (OLS). The thermal method, based
9 on the cantilever's thermal fluctuations in fluid, allows estimating k_c in a fast, non-invasive mode. How-
10 ever, differences in the cantilever geometry and mounting angle require the knowledge of three correction
11 factors to get a good estimation of k_c : the contribution of the oscillation mode to the total amplitude, the
12 shape difference between the free and the end-loaded configurations, and the tilt of the cantilever respect
13 to the measured surface. While the correction factors for traditional rectangular and V-shaped cantilevers
14 geometries have been reported, they must be determined for cantilevers with non-traditional geometries and
15 large tips. Here, we develop a method based on finite element analysis to estimate the correction factors of
16 cantilevers with arbitrary geometry and tip dimensions. The method relies on the numerical computation
17 of the effective cantilever mass. The use of the correction factor for rectangular geometries on our model
18 cantilever (PFQNM-LC) will lead to values underestimated by 16%. In contrast, experiments using pre-
19 calibrated cantilevers revealed a maximum uncertainty below 5% in the estimation of the OLS , verifying
20 our approach.

* jorge.r.ramos@outlook.com

21 I. INTRODUCTION

22 Atomic force microscopy (AFM) has evolved and diversified since its invention in 1986 [1].
23 A mainstream application of AFM is devoted to force spectroscopy measurements to probe the
24 mechanics of materials, including biological systems, such as protein unfolding, receptor-ligand
25 interactions, and the mechanical properties of cells [2–10].

26 In a typical AFM setup, a laser beam reflects in the cantilever’s back to monitor the deflection
27 from the change in the position of the reflected light on a segmented photodiode. To obtain ac-
28 curate force measurements, it is crucial to know the conversion factor to transform the electrical
29 signal read in the photodiode (in volts) into the actual displacement (typically nanometers). The
30 more straightforward method to obtain the conversion factor is to deflect the cantilever against a
31 hard surface by obtaining force-distance (FD) curves. Knowing the scanner movement in the ver-
32 tical direction, the slope of the voltage change of the photodiode provides the conversion factor or
33 optical lever sensitivity (*OLS*), and its inverse (*invOLS* = $\Delta z/\Delta V$) [11]. The *invOLS* value allows
34 estimating the spring constant by the thermal method from the fundamental mode of oscillation of
35 the cantilever [11–16]

$$36 \quad k_c = \frac{\beta}{\chi^2} \frac{k_B T}{invOLS^2 \langle V^2 \rangle} \quad (1)$$

37 where k_B is the Boltzmann constant, T is the absolute temperature, $\langle V^2 \rangle$ is the mean-square
38 deflection in volts due to thermal fluctuations of the fundamental mode. The β factor corrects
39 the difference between the spring constant of the cantilever (or static spring constant) from that
40 of the fundamental mode k_1 (or k dynamic). The factor χ corrects the difference in the measured
41 deflection of the end-loaded cantilever, respect to the freely oscillating cantilever. Finally, the
42 cantilever’s mean square displacement is $\langle z_c^2 \rangle = \chi^2 invOLS^2 \langle V^2 \rangle$. Since pushing the cantilever tip
43 against a hard surface is not always possible and may damage the tip, the calibration of both, the
44 spring constant and the *invOLS* based on the thermal method is becoming popular in biological
45 AFM applications [11, 16–19].

46 The analytical values of χ and β , for rectangular cantilevers with a tip of despicable mass and
47 a laser spot infinitely small located at the free end are vastly known [11–16, 20]. However, can-
48 tilever geometries are moving towards more irregular shapes. For example, PFQNM-LC-A-CAL
49 cantilevers (PFQNM hereafter, Bruker) feature paddle-like geometry to reduce viscous damping
50 [21] and have a very large tip, compared to the cantilever size (Fig. 1). The correction factors of

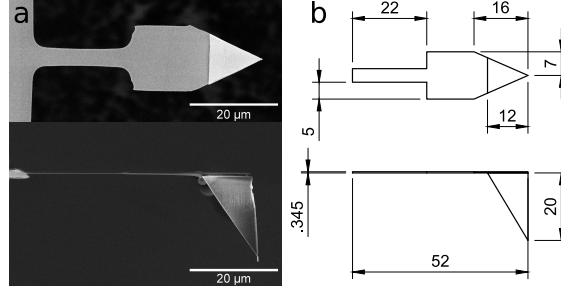


FIG. 1. PFQNM cantilever. (a) Scanning electron micrographs of the bottom and lateral views. (b) Relevant dimensions of the simplified geometry used in the simulations by FEA.

51 PFQNM cantilevers should differ from those of the rectangular beam. On the other hand, man-
 52 ufacturers provide the spring constant's precalibrated values, allowing calibration of the *invOLS*
 53 using either FD curves on a hard substrate or thermal analysis. PFQNM cantilevers feature a large
 54 pyramidal tip of $\sim 20 \mu\text{m}$ height with a protruding rounded cylinder of $\sim 70 \text{ nm}$ radius, being
 55 resistant, in principle, to FC-based calibration. Nonetheless, for cantilevers with tip functional-
 56 ization or with sharp tips (e.g., PEAKFORCE-HIRS-F family, Bruker), samples placed on a soft
 57 surface [22], or samples covering all the sample surface (e.g., tissue [23, 24], confluent cells or
 58 extracellular matrix [25]), may not allow FC-based calibration. Thus, it is more convenient to
 59 use the thermal method (Eq. 1) to calibrate the *invOLS*. This requires accurate knowledge of the
 60 correction factors χ and β for the type of cantilever used. However, analytical expressions for β
 61 and χ are only available for rectangular geometries.

62 There is an important correction to include in Eq. 1. In most AFM experimental setups, the
 63 cantilever is mounted at an angle $\theta = 10$ to 12 degrees with respect to the horizontal plane. It's
 64 been noticed that the effective spring constant of the tilted cantilever (k_θ) is different from k_c
 65 (non-tilted). The effective stiffness of a cantilever with a despicable tip mass, loaded at the end
 66 will increase by $1/\cos^2 \theta$ [13, 20, 26]. When the tip size is large (e.g., PFQNM or colloidal
 67 probes), additional corrections are needed [27, 28]. Although there are analytical expressions for
 68 its calculation on rectangular cantilevers, this correction is not well defined for cantilevers and tips
 69 of irregular geometry.

70 Finite element analysis (FEA) is a common alternative to derive the cantilever's mechanical
 71 properties when analytical solutions do not exist. For example, Stark et al. [12] used FEA to
 72 determine the χ and β factors from V-shaped cantilevers. While it is relatively simple to extract
 73 χ using FEA, to our knowledge, there is no clear method to determine β . Here, we implement a

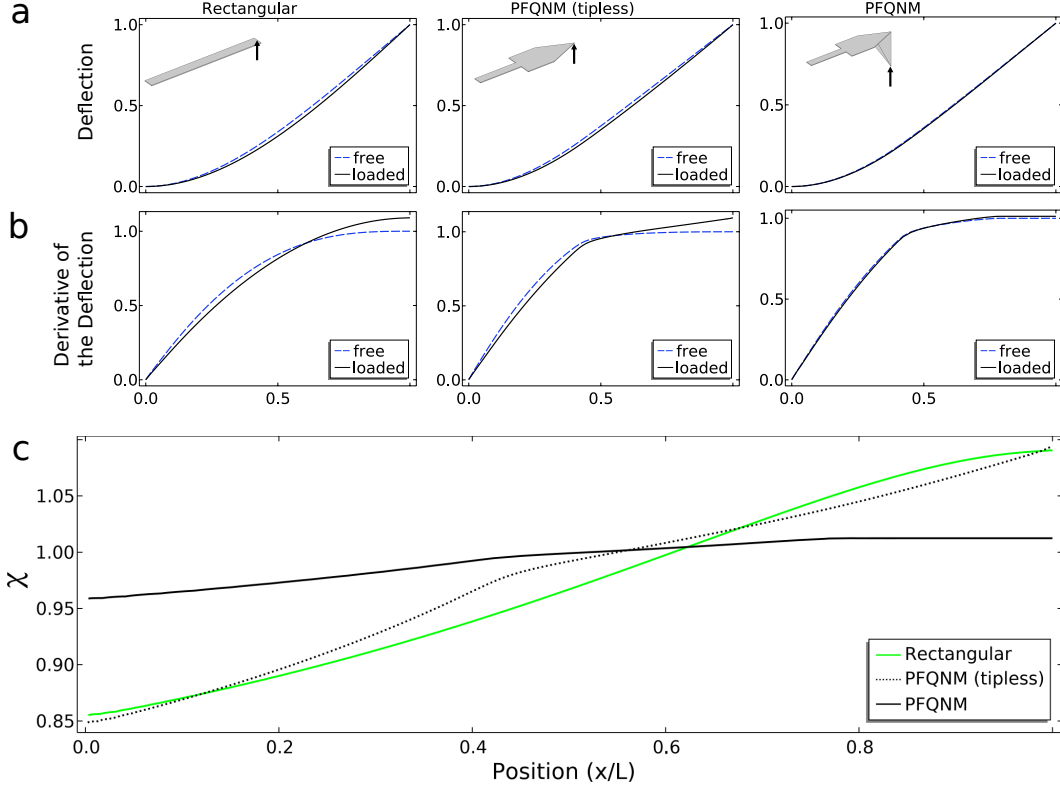


FIG. 2. Determination of the correction factor χ in COMSOL. (a) Deflection of the free and the end-loaded cantilevers, obtained from the eigenmode and stationary studies, respectively. The inset represents the geometry of the cantilever, fixed at $x = 0$. The arrow represents the point where the load force is applied (stationary study). (b) Derivative of the deflection. (c) Correction factor χ (Eq. 6). See χ along the cantilever axis for additional geometries in supplementary Fig. S2.

74 method based on FEA to determine the effective mass to calculate β for cantilevers of arbitrary
 75 shape. Our approach includes the determination of the tilt correction factor and the adjustment of
 76 the manufacturer's pre-calibrated spring constant, to adapt it to our experimental conditions. We
 77 apply the method to cantilevers with different geometries and validate it experimentally.

78 II. FINITE ELEMENT ANALYSIS

79 We used COMSOL Multiphysics version 5.5 (COMSOL hereafter) to perform the FEA mod-
 80 eling [29]. The analysis was applied to a classical cantilever with a homogeneous rectangular
 81 section, the simplified PFQNM showed in Fig. 1b and a version of PFQNM without the tip (rect-
 82 angular, PFQNM and tipless PFQNM cantilevers hereafter). The rectangular cantilever had the

83 dimensions of the PFQNM cantilever provided by the manufacturer in the cantilever's box: length
84 of $54 \mu\text{m}$, width of $4.5 \mu\text{m}$ and thickness $0.345 \mu\text{m}$. The actual dimensions of the PFQNM levers
85 were extracted from scanning electron microscopy micrographs (Teneo VS, FEI) and are shown in
86 Fig. 1. For simplicity, the modelled material was silicon with Young's modulus $E = 170 \text{ MPa}$ and
87 density $\rho = 2329 \text{ kg/m}^3$. See supplementary Fig. S1 for geometrical details of the other simulated
88 geometries. To determine both β and χ factors, we run two FEA studies: a static simulation in
89 which a vertical load was applied at tip position (insets, Fig. 2a) to determine the deflection of the
90 end-loaded cantilever, and an eigenfrequency simulation to determine resonance frequency and
91 the modal shape of the free cantilever in vacuum. Here, we will refer to the results of the static
92 and eigenfrequency studies as 'loaded' and 'free' modelling solutions.

93 A. Determination of the correction factors β and χ

94 The factor β is defined as

$$95 \quad \beta = \frac{k_c}{k_1} \quad (2)$$

96 For a rectangular cantilever, $\beta = 0.971$ as determined analytically and from FEA [11, 13–15].
97 In the static study, We obtain k_c by Hooke's law

$$98 \quad k_c = \frac{F_z}{z_l} \quad (3)$$

99 where F_z is the vertical load applied and z_l is the vertical deflection at the point of force application.

100 In the eigenfrequency study, the fundamental mode of oscillation has a resonance frequency f_1
101 that is related to the dynamic spring constant k_1 by

$$102 \quad k_1 = m_e(2\pi f_1)^2 \quad (4)$$

103 where m_e is the effective mass of the cantilever at the resonance frequency, which is $0.25m_c$ for the
104 rectangular cantilever [15, 30], but may differ for a cantilever with irregular geometry and large
105 tip dimensions. We used the method proposed by Hauer et al. [30] to define the effective mass
106 integral

$$107 \quad m_e(x_l) = \frac{1}{|r_1(x_l)|^2} \int_V dV \rho(x) |r_1(x)|^2 \quad (5)$$

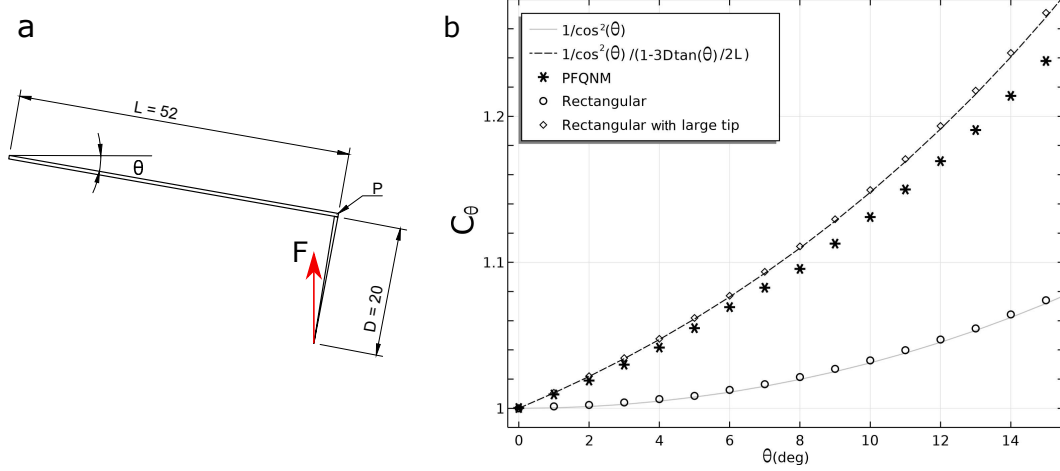


FIG. 3. Cantilever tilt correction factor C_θ (Eq. 7). (a) Schematic of a rectangular cantilever with a long sharp tip, with the same tip height and cantilever length as the PFQNM modelled in this work (Fig. 1a). The force F is applied at the very end. The spring constant is determined at point P, located within the cantilever body. (b) FEA calculated values for the classical rectangular cantilever (tip-less), the rectangular cantilever with idealised long sharp tip (a) and the PFQNM cantilever. The gray solid line represents the theoretical value for a rectangular cantilever $1/\cos^2 \theta$, while the black dashed line is the theoretical value for a cantilever with a sharp large tip (Eq. 11).

108 where ρ is the density and r_1 is the first mode shape solution along the longitudinal axis (x); x_l
 109 represents the position where the load F_z is applied (i.e., at the tip position). This approach was
 110 validated by the calibration values obtained for V-shaped cantilevers (Table I), where the force
 111 is not applied at the free end. Indeed, the work of Hauer [30] suggests that the effective mass
 112 is a function of the position at which we measure the device; in our case, at the point where
 113 the load is applied. Importantly, Eq. 5 applies to geometries of arbitrary shape and we solved it
 114 numerically for the different cantilever geometries using COMSOL. As expected, we obtained the
 115 same analytical value of m_e of 0.25 of the cantilever mass (m_c) for the rectangular cantilever.

116 To obtain χ , we determined the derivative the deflection along the cantilever longitudinal axis
 117 of the loaded and free solutions and computed their quotient

$$118 \quad \chi = \frac{\text{invOLS}_{free}}{\text{invOLS}} = \frac{\frac{d}{dx}(z_{loaded})}{\frac{d}{dx}(z_{free})} \quad (6)$$

119 where z_{loaded} and z_{free} are the vertical deflection of the loaded and free solutions, respectively.
 120 For a rectangular cantilever, we obtained $\chi = 1.09$, as reported before, using analytical and FEA

121 approaches [11, 13, 15, 31] (Table I).

122 1. *PFQNM cantilevers*

123 The values of m_e , β and χ obtained for different cantilever geometries are shown in Table I.
124 We also report, as reference, the values for geometries reported in the literature that confirm our
125 approach (such as V-shaped MLCT-D, Bruker and arrow-shaped AC160TS, Olympus)[12, 32]. As
126 shown in Fig. 2a, b, for the rectangular and the tipless PFQNM cantilevers, the deflection of the
127 freely oscillating cantilever is different from the deflection of the end-loaded; the same applies for
128 the deflection's derivative. However, this difference is less pronounced in the case of the PFQNM
129 (including the tip). This suggests that the mass of the PFQNM cantilever tip (which accounts for
130 approximately 60 to 75% of the cantilever's total mass, see supplementary Table S1) has a strong
131 influence in its mechanical behaviour. The consequence is a factor χ much closer to 1 for the
132 PFQNM cantilever with respect to the other two cantilever types (Fig. 2c and Table I). In addition,
133 the χ factor remains approximately the same for the last 20% of its length towards the free end.
134 This implies that force measurements will be less affected by little changes in the position of the
135 laser spot.

136 Despite obvious geometrical differences, the values of χ and β for the tipless PFQNM can-
137 tilever are within $\sim 0.5\%$ from the rectangular ones (Table I). However, the χ and β values for
138 the PFQNM cantilever, including its large tip, differ importantly from the rectangular ones; the
139 PFQNM values are 7.7% lower (χ) and 2.8% higher (β). Thus, using the rectangular correction
140 factors to calibrate the *invOLS* from Eq. 4 on a PFQNM cantilever will lead to a non-negligible
141 $\sim 16\%$ error in the estimation of the *invOLS* and, subsequently, in the determination of the mea-
142 sured forces.

143 2. *V-shaped cantilevers*

144 Regarding V-shaped cantilevers, the correction factors χ and β were estimated by Stark et al.
145 [12] for, at the time, the Thermomicroscopes type E cantilever, with similar dimensions to the
146 MLCT-E from Bruker (Table I). Our simulated values are very close to those reported before
147 and are similar (within $\sim 1\%$) between MLCT-D and E. However, it is important to note that the
148 calibration parameters will depend on the position of the tip. Even for MLCT cantilevers within

TABLE I. Estimated parameters of selected cantilevers.

Cantilever	m_e/m_c	β	χ^a	β/χ^2
Rectangular, analytical ^b	0.250	0.971	1.090	0.8175
Rectangular	0.249	0.971	1.090	0.8173
PFQNM (tipless)	0.264	0.966	1.094	0.8068
PFQNM ^c	0.631	0.998	1.012	0.9737
MLCT-E like, Ref. [12]	–	0.963	1.125	0.7608
MLCT-E, V-shaped	0.232	0.956	1.125	0.7554
MLCT-D, V-shaped	0.227	0.959	1.116	0.7690
AC160TS, Ref. [32]	–	0.908	1.254	0.5776
AC160TS (tipless)	0.151	0.904	1.271	0.5600
AC160TS	0.156	0.915	1.217	0.6177

^a χ value at the end of the cantilever.

^b See references [11, 13–15].

^c See supplementary Table S1 for simulations considering a the reflective gold coating on the cantilever’s back.

149 the same chip, where the distance to the tip-end is the same (in our case, $7 \mu\text{m}$), the relative
150 position of the tip will be different for different cantilevers dimensions (A to F).

151 3. AC160TS cantilevers

152 AC160TS cantilevers, which have been simulated by FEA before [33, 34], constitute another
153 interesting example to assess the importance of the tip mass. Our simulations of an AC160TS
154 cantilever without the tip, are close to the values reported in the literature (Table I). However,
155 when we include the tip on the simulation, the correction factor χ/β^2 increases by 10%. Overall,
156 the tip of the AC160 is almost as large as that of the PFQNM (see supplementary information),
157 but its influence is smaller because its mass represent only 1% of the total mass.

158 It is important to note that the χ values shown in Table I correspond to the end of the cantilever.

159 However, it is common to place the laser spot before the end. This translates into a χ smaller than
 160 χ at the end [31, 34]. We show the χ values along the x axis of the cantilevers in Fig. S2.

161 B. Cantilever tilt

162 In general, the relationship between the spring constant of the non-tilted cantilever k_c , and the
 163 effective spring constant k_θ of the same cantilever, mounted with an angle θ in the AFM system is

$$164 \quad k_\theta = C_\theta k_c \quad (7)$$

165 where the factor C_θ will depend on the tilt angle and the tip's geometry and position [27].

166 By substituting Eq. 7 in Eq. 1 we get an equation for the tilted cantilever

$$167 \quad k_\theta = \frac{\beta}{\chi^2} \frac{C_\theta}{invOLS^2} \frac{k_B T}{\langle V^2 \rangle} = \beta C_\theta \frac{k_B T}{\langle z_c^2 \rangle} \quad (8)$$

168 If we define the effective *invOLS* of the tilted cantilever as

$$169 \quad invOLS_\theta = \frac{invOLS}{\sqrt{C_\theta}} \quad (9)$$

170 we can rewrite Eq. 8 to estimate the effective spring constant when using the $invOLS_\theta$ from static
 171 force curves, without need to correct the tilting or the cantilever geometry

$$172 \quad k_\theta = \frac{\beta}{\chi^2} \frac{k_B T}{invOLS_\theta^2 \langle V^2 \rangle} \quad (10)$$

173 1. Determination of the tilt correction factor C_θ by FEA

174 We need to implement Eq. 7 to determine the correction factor C_θ by FEA. Figure 3a shows a
 175 rectangular cantilever with a large tip. The lever is tilted an angle θ respect to the horizontal. The
 176 force is applied at the very end of the cantilever. The spring constant is determined by the Hooke's
 177 law (Eq. 3) in the point P (perpendicular to the point of application of the force in the reference
 178 system of the cantilever). The theoretical C_θ value for the cantilever-tip system depicted in Fig. 3a
 179 [26, 27] is

$$180 \quad C_\theta = \left[\cos^2 \theta \left(1 - \frac{3D}{2L} \tan \theta \right) \right]^{-1} \quad (11)$$

181 where D is the tip height and L the cantilever's length.

182 Figure 3b shows the simulated values of C_θ for three geometries. There is a very good agree-
183 ment between the simulated and the theoretical value for the bare rectangular cantilever ($D = 0$).
184 The same occurs for the rectangular cantilever with the long tip and the theoretical value from
185 Eq 11. However, C_θ for the PFQNM cantilever deviates from Eq 11, even though the ratio D/L is
186 the same as for the idealized cantilever with long tip in Fig 3a. Possible reasons for this difference
187 are the paddle geometry of the cantilever or the larger zone of interaction between cantilever and
188 the base of the pyramidal tip.

189 2. Practical implementation using manufacturer pre-calibrated cantilevers

190 The spring constant of PFQNM probes is pre-calibrated by the manufacturer. The mean square
191 displacement $\langle z_c^2 \rangle$ of each cantilever is determined by using a laser Doppler vibrometer (LDV)
192 as described by Ohler [13]. For simplicity, the manufacturers do not consider the tip height in
193 the calibration process (i.e., $D = 0$ in Eq. 11). In that case, the equation used to determine the
194 pre-calibrated spring constant k_{cal} is

$$195 \quad k_{\text{cal}} = \frac{\beta}{\cos^2 \theta} \frac{k_B T}{\langle z_c^2 \rangle} = 1.0149 \frac{k_B T}{\langle z_c^2 \rangle} \quad (12)$$

196 where $\beta = 0.971$ (rectangular cantilever) and $\theta = 12^\circ$, the most common tilt angle in Bruker AFM
197 systems.

198 Since the mean square displacement of the cantilever $\langle z_c^2 \rangle$ should be the same regardless the
199 measuring technique, we can combine Eq. 8 and Eq. 12 to obtain a 'corrected' value of the pre-
200 calibrated spring constant for our AFM system

$$201 \quad k_{\text{corr}} = \frac{\beta C_\theta}{1.0149} k_{\text{cal}} \quad (13)$$

202 Note that for a rectangular cantilever with tip of despicable mass $k_{\text{corr}} = k_{\text{cal}}$. In our experimen-
203 tal conditions, we used PFQNM cantilevers $\beta = 0.998$ (Table I) mounted in a Nanowizard 4 AFM
204 system with $\theta = 10^\circ$, then $C_\theta = 1.131$ (Fig. 3b), and $k_{\text{corr}} = 1.1122 k_{\text{cal}}$ (i.e., the effective stiffness
205 of PFQNM cantilevers is expected to be $\sim 11\%$ higher than the calibrated value provided by the
206 manufacturer).

207 The effective *invOLS* based on the pre-calibrated spring constant provided by the manufacturer

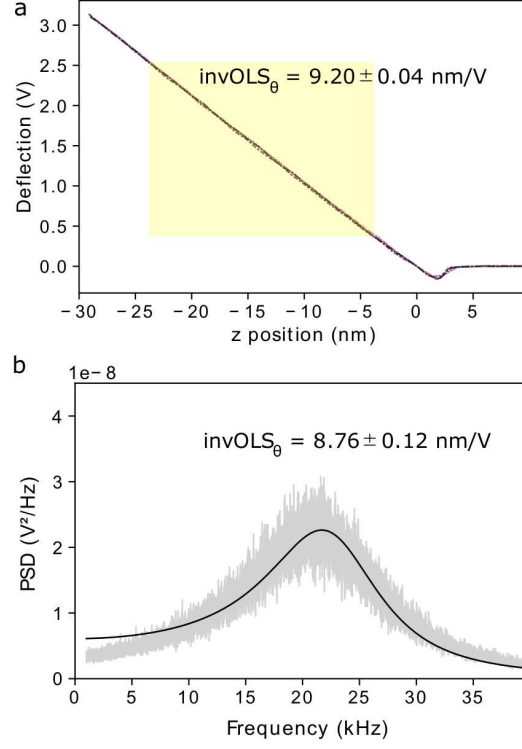


FIG. 4. Experimental determination of the effective $invOLS$ of cantilever No. 1 in Table II. (a) Overlap of five force curves on a rigid surface, in liquid media. The $invOLS_{\theta}$ is the inverse of the slope of the linear region of the force curves. The fitting was performed in the center of the zone of interest, between 0.5 and 2.5 V (shaded region). (b) $invOLS_{\theta}$ estimation from thermal spectra in liquid (Eq. 14), ($n = 5$).

208 will be

$$209 \quad invOLS_{\theta} = \sqrt{\frac{1.0149}{\chi^2 C_{\theta}} \frac{k_B T}{k_{cal} \langle V^2 \rangle}} \quad (14)$$

210 3. Practical implementation using cantilevers calibrated by Sader's method

211 The Sader method is widely used to determine the spring constant of a large number of com-
 212 mercial cantilevers [18, 33, 35]. In this case, the effective $invOLS$ would be determined by

$$213 \quad invOLS_{\theta} = \sqrt{\frac{\beta}{\chi^2 C_{\theta} k_{Sader}} \frac{k_B T}{\langle V^2 \rangle}} \quad (15)$$

TABLE II. Experimental determination of the effective *invOLS* and effective spring constant of PFQNM cantilevers.^a

Lever No.	<i>invOLS</i> _θ (nm/V)		<i>k</i> _θ (mN/m)	
	static ^b	thermal (Rel. error) ^c	corrected ^d	estimated (Rel. error) ^e
1	9.20 0.04	8.76 0.12 (-4.8%)	129	117 3 (-9.3%)
2	9.12 0.31	8.96 0.06 (-1.7%)	107	103 1 (-3.7%)
3	9.12 0.20	8.68 0.03 (-4.9%)	103	94 1 (-8.7%)

^a Values reported as mean ± standard deviation.

^b Based on force curves in rigid surface (Fig. 4a).

^c Based on thermal noise spectra (Fig. 4b, Eq. 14).

^d Corrected value of the manufacturer's spring constant (Eq. 13).

^e Equation 10.

214 III. EXPERIMENTAL VALIDATION

215 To further verify our FEA approach, we experimentally determined the *invOLS* using both
 216 thermal and FC-based methods on three PFQNM cantilevers with pre-calibrated spring con-
 217 stant (Bruker). Experiments were performed in a commercial AFM system (JPK Nanowizard 4,
 218 Bruker). For each cantilever, three thermal spectra were recorded in liquid media (10 mM Tris,
 219 150 mM KCl, pH 7.4, Merck), keeping the cantilevers more than 500 μm away from a freshly
 220 cleaved mica surface. Then, five force curves were acquired on the mica surface to a force setpoint
 221 of 3 V, which guaranteed to have a sufficiently wide linear region to determine the *invOLS* around
 222 the center of the photodiode Fig. 4a. Finally, three new spectra were recorded far from the surface.
 223 The thermal spectra were fitted with the damped simple harmonic oscillator (SHO) model

$$224 \quad S = A_w^2 + \frac{A^2 f_1^4}{Q^2} \left[(f^2 - f_1^2) + \frac{f^2 f_1^2}{Q^2} \right]^{-1} \quad (16)$$

225 where A_w is the background noise, A is the amplitude at the resonance frequency (f_1), and Q is the
 226 quality factor (Fig. 4b). Then, we calculated the mean-squared deflection in volts as [16]

$$227 \quad \langle V^2 \rangle = \frac{\pi A^2 f_1}{2Q} \quad (17)$$

228 The *invOLS*_θ was recovered by substituting Eq. 17 into Eq. 14, using the pre-calibrated spring
 229 constant. The results are summarized in Table II. Even if the five force curves were performed

230 micrometres away from each other, they were almost indistinguishable when aligned to zero force
231 (Fig. 4a), resulting in $\sim 2\%$ average uncertainty. Overlapping was also observed in the thermal
232 spectra (Fig. 4b), even if those were recorded before and after the force curves acquisition, result-
233 ing in even lower uncertainty $< 1\%$.

234 For the three cantilevers measured, we found a good agreement between the $invOLS_\theta$ derived
235 from the force curves and from the thermal spectra. Note that, since we have the calibrated value
236 from the manufacturer, the factor β does not appear in Eq. 14. We obtained a relative difference
237 $\sim 4\%$ on average, far below the 16% uncertainty using the correction χ and β for rectangular
238 cantilevers. We obtained SEM images of all three PFQNM cantilevers and tips after the AFM
239 experiments to accurately determine their geometry, finding small variability between cantilevers
240 and tips (Fig. S3).

241 The comparison of the ‘corrected’ value of the spring constant with the calculated stiffness
242 using $invOLS_\theta$ from static force curves (Eq. 10) leads to a fairly good agreement (the average is
243 $\sim 7\%$, Table II). As has been shown before, these results suggest that the thermal determination
244 of the $invOLS$ leads to less uncertainty (1/2) compared to the classical approach [19].

245 If the experiments are performed under optimal conditions on a clean hard surface, and the
246 vertical movement of the piezo-scanner is well calibrated, the actual $invOLS_\theta$ value is the one
247 obtained from slope of the force curves. The difference in values could be due to the influence
248 of the reflective coating on the cantilever mass (see supplementary Table S1), small geometrical
249 differences between cantilevers of different batches, the calibration of the piezo-scanner or the
250 values reported by the manufacturer; these two last factors were considered to be error-free in the
251 calculations shown in Table II.

252 In summary, we implemented a finite element analysis method to determine the correction
253 factors χ , β and C_θ to calibrate the spring constant and the $invOLS$ by the thermal tune method.
254 Our simulations agree with the values reported in classical geometries, like the rectangular and
255 the V-shaped, which suggests the method is valid for arbitrary shape. As relevant case within non-
256 standard geometries, we focused on PFQNM cantilevers, characterized by a paddle shape with a
257 large tip relative to the cantilever dimensions. We found that a beneficial effect of the massive tip is
258 the little variation in the correction factor χ near its free end. Thus, laser positioning changes will
259 produce a little variation of χ , resulting in more robust experimental results. In addition to that,
260 our method provides a ‘correction’ to the pre-calibrated value provided by the manufacturer. We
261 found a good agreement between the effective $invOLS$ obtained from force curves and the thermal

262 tune method in AFM experiments with PFQNM cantilevers, confirming the approach's validity.

263 SUPPLEMENTARY MATERIAL

264 See supplementary material for additional cantilever geometries, correction factors χ for the
265 cantilevers studied and additional simulations of PFQNM cantilevers, considering the reflective
266 gold layer coating.

267 ACKNOWLEDGMENTS

268 We thank Alexander Dulebo (Bruker) for kindly providing technical information and Alessan-
269 dro Podestà and Matteo Chighizola for insightful discussions. The electron microscopy experi-
270 ments were carried on the PICsL-FBI core electron microscopy facility (Nicolas Brouilly, IBDM,
271 AMU-Marseille UMR 7288), member of the national infrastructure France-BioImaging supported
272 by the French National Research Agency (ANR-10-INBS-0004). This project has received fund-
273 ing from the European Research Council (ERC, grant agreement No 772257).

274 DATA AVAILABILITY

275 The data that support the findings of this study are available from the corresponding author
276 upon reasonable request.

-
- 277 [1] G. Binnig, C. F. Quate, and C. Gerber, *Physical Review Letters* **56**, 930 (1986).
278 [2] M. Radmacher, R. Tillmann, M. Fritz, and H. Gaub, *Science* **257**, 1900 (1992).
279 [3] V. T. Moy, E.-L. Florin, and H. E. Gaub, *Colloids and Surfaces A: Physicochemical and Engineering*
280 *Aspects* **93**, 343 (1994).
281 [4] M. Radmacher, M. Fritz, C. M. Kacher, J. P. Cleveland, and P. K. Hansma, *Biophysical Journal* **70**,
282 556 (1996).
283 [5] M. Rief, F. Oesterhelt, B. Heymann, and H. E. Gaub, *Science* **275**, 1295 (1997).
284 [6] M. Lekka, K. Pogoda, J. Gostek, O. Klymenko, S. Prauzner-Bechcicki, J. Wiltowska-Zuber,
285 J. Jaczewska, J. Lekki, and Z. Stachura, *Micron* **43**, 1259 (2012).

- 286 [7] J. R. Ramos, J. Pabijan, R. Garcia, and M. Lekka, *Beilstein journal of nanotechnology* **5**, 447 (2014).
- 287 [8] M. L. Hughes and L. Dougan, *Reports on Progress in Physics* **79**, 076601 (2016).
- 288 [9] W. Ott, M. A. Jobst, C. Schoeler, H. E. Gaub, and M. A. Nash, *Journal of Structural Biology* **197**, 3
289 (2017).
- 290 [10] C. Valotteau, F. Sumbul, and F. Rico, *Biophysical Reviews* **11**, 689 (2019).
- 291 [11] S. M. Cook, T. E. Schäffer, K. M. Chynoweth, M. Wigton, R. W. Simmonds, and K. M. Lang,
292 *Nanotechnology* **17**, 2135 (2006).
- 293 [12] R. W. Stark, T. Drobek, and W. M. Heckl, *Ultramicroscopy* **86**, 207 (2001).
- 294 [13] B. Ohler, *Spring AN94*, 1 (2007).
- 295 [14] H.-J. Butt, B. Cappella, and M. Kappl, *Surface Science Reports* **59**, 1 (2005).
- 296 [15] R. Garcia, *Amplitude Modulation Atomic Force Microscopy*, 1st ed. (Wiley-VCH Verlag, 2010) Chap.
297 179.
- 298 [16] F. Sumbul, N. Hassanpour, J. Rodriguez-Ramos, and F. Rico, *Frontiers in Physics* **8**, 301 (2020).
- 299 [17] H. J. Butt and M. Jaschke, *Nanotechnology* **6**, 1 (1995).
- 300 [18] M. J. Higgins, R. Proksch, J. E. Sader, M. Polcik, S. Mc Endoo, J. P. Cleveland, and S. P. Jarvis,
301 *Review of Scientific Instruments* **77**, 1 (2006).
- 302 [19] H. Schillers, C. Rianna, J. Schäpe, T. Luque, H. Doschke, M. Wälte, J. J. Uriarte, N. Campillo, G. P.
303 Michanetzis, J. Bobrowska, A. Dumitru, E. T. Herruzo, S. Bovio, P. Parot, M. Galluzzi, A. Podestà,
304 L. Puricelli, S. Scheuring, Y. Missirlis, R. Garcia, M. Odorico, J. M. Teulon, F. Lafont, M. Lekka,
305 F. Rico, A. Rigato, J. L. Pellequer, H. Oberleithner, D. Navajas, and M. Radmacher, *Scientific Reports*
306 **7**, 1 (2017).
- 307 [20] B. Ohler, *Review of Scientific Instruments* **78**, 063701 (2007).
- 308 [21] D. T. Edwards, J. K. Faulk, M.-A. LeBlanc, and T. T. Perkins, *Biophysical journal* **113**, 2595 (2017).
- 309 [22] J. Solon, I. Levental, K. Sengupta, P. C. Georges, and P. A. Janmey, *Biophysical Journal* **93**, 4453
310 (2007).
- 311 [23] M. Lekka, D. Gil, K. Pogoda, J. Dulińska-Litewka, R. Jach, J. Gostek, O. Klymenko, S. Prauzner-
312 Bechcicki, Z. Stachura, J. Wiltowska-Zuber, K. Okoń, and P. Laidler, *Archives of Biochemistry and*
313 *Biophysics* **518**, 151 (2012).
- 314 [24] M. Plodinec, M. Loparic, C. A. Monnier, E. C. Obermann, R. Zanetti-Dallenbach, P. Oertle, J. T.
315 Hyotyła, U. Aebi, M. Bentires-Alj, Y. H. LimRoderick, and C.-A. Schoenenberger, *Nature Nanotech-*
316 *nology* **7**, 757 (2012).

- 317 [25] J. Goetz, S. Minguet, I. Navarro-Lérida, J. Lazcano, R. Samaniego, E. Calvo, M. Tello, T. Osteso-
318 Ibáñez, T. Pellinen, A. Echarri, A. Cerezo, A. P. Klein-Szanto, R. Garcia, P. Keely, P. Sánchez-Mateos,
319 E. Cukierman, and M. Del Pozo, *Cell* **146**, 148 (2011).
- 320 [26] J. L. Hutter, *Langmuir* **21**, 2630 (2005).
- 321 [27] S. A. Edwards, W. A. Ducker, and J. E. Sader, *Journal of Applied Physics* **103**, 064513 (2008).
- 322 [28] M. Chighizola, L. Puricelli, L. Bellon, and A. Podestà, *Journal of Molecular Recognition* **34** (2021),
323 10.1002/jmr.2879.
- 324 [29] COMSOL Multiphysics v. 5.5., www.comsol.com., COMSOL AB, Stockholm, Sweden,.
- 325 [30] B. D. Hauer, C. Doolin, K. S. D. Beach, and J. P. Davis, *Annals of Physics* **339**, 181 (2013).
- 326 [31] R. Proksch, T. E. Schäffer, J. P. Cleveland, R. C. Callahan, and M. B. Viani, *Nanotechnology* **15**, 1344
327 (2004).
- 328 [32] J. E. Sader, J. Lu, and P. Mulvaney, *Review of Scientific Instruments* **85**, 113702 (2014).
- 329 [33] J. E. Sader, J. A. Sanelli, B. D. Adamson, J. P. Monty, X. Wei, S. A. Crawford, J. R. Friend, I. Marusic,
330 P. Mulvaney, and E. J. Bieske, in *Review of Scientific Instruments*, Vol. 83 (2012) p. 103705.
- 331 [34] J. E. Sader, M. Yousefi, and J. R. Friend, *Review of Scientific Instruments* **85**, 025104 (2014).
- 332 [35] J. E. Sader, R. Borgani, C. T. Gibson, D. B. Haviland, M. J. Higgins, J. I. Kilpatrick, J. Lu, P. Mulvaney,
333 C. J. Shearer, A. D. Slattery, P.-A. Thorén, J. Tran, H. Zhang, H. Zhang, and T. Zheng, *Review of*
334 *Scientific Instruments* **87**, 093711 (2016).

